

# Real-Time Models of Electrostatically Actuated Cantilever Probes With Integrated Thermal Sensor for Nanoscale Interrogation

Pranav Agarwal, Deepak R. Sahoo, Abu Sebastian, *Member, IEEE*,  
Haris Pozidis, *Member, IEEE*, and Murti V. Salapaka

**Abstract**—Microcantilevers with integrated thermal sensor for topography measurement, which can be electrostatically actuated, are well suited for a highly parallel dynamic-mode operation where multiple cantilevers scan the media. Interpretation of data in dynamic-mode operation utilizing such cantilevers is complex because of diverse forces acting on the cantilever that include electrostatic, interatomic, structural, thermal, and, possibly, magnetic forces. In addition, the thermal sensor introduces new dynamics making interpretation of measured data challenging. In this paper, tractable models that are suited for real-time purposes, which can quantitatively predict the cantilever motion and the thermal-sensor measurement, are presented. Furthermore, it is demonstrated that all parameters of the model can be estimated solely from thermal-sensor data. This paper also provides a comprehensive understanding of the dynamics of the thermal sensor. [2009-0041]

**Index Terms**—Characterization, data storage, dynamic mode, electrostatic actuation, microcantilever, microheater, millipede, modeling, probe-based, tapping mode, thermal sensing.

## I. INTRODUCTION

THE IMPORTANCE of cantilevers with integrated thermal sensors is exemplified by a variety of applications, viz., calorimetry [1], thermal dip-pen lithography [2], thermal metrology [3], [4], room-temperature chemical vapor deposition [5], microfluidic actuation [6], thermomechanical actuation [7], local thermal property measurements [8], and high-density data storage [9]. Typical thermomechanical cantilevers rely on the dependence of the resistance of an electrical path on the temperature of the surrounding environment. For example, in probe-based data storage, the separation of the media from the cantilever determines the heat transfer from the cantilever to the media, which in turn determines the resistance of the electrical path. In addition, most of the resistance of the electrical path is typically concentrated in a small region, which is achieved by differentially doping cantilever legs (see Fig. 1). This region

is termed as the *thermal sensor* in this paper. As the resistance of the electrical path is primarily determined by the thermal sensor, the current through the electrical path is primarily determined by the thermal sensor. We define this current as the thermal-sensor output. Various studies that research heat-transfer processes which affect the thermal conduction pathway from the cantilever to the sample are reported in [10]–[18].

In most present operation schemes, cantilevers are operated in contact mode where the cantilever dynamics do not play a significant role, and the thermal-sensor output is interpreted in a quasi-static sense. Operation in contact mode leads to significant tip-sample wear due to high lateral forces. It is known (see [19] and [20]) that in dynamic-mode operation where the cantilever is in intermittent contact mode with the sample, frictional forces between the media and the cantilever are smaller, resulting in considerable reduction of tip and media wear. An attractive method of obtaining such an operation is to oscillate the cantilever by inducing a changing voltage between the media surface and the cantilever, producing a changing electrostatic force on the cantilever.

In dynamic intermittent contact operation with electrostatic actuation, cantilever trajectories result from the interaction of cantilever-beam mechanics with electrostatic, Van der Waals, and adhesive forces. In addition, the current through the cantilever for certain cantilever geometries can be influenced by capacitive and magnetic effects that can make the interpretation of the thermal-sensor output challenging. Thus, the complexity of quantitatively predicting the cantilever motion and the associated thermal-sensor output is considerable.

In this paper, a characterization of time constants of various physical processes with the ability of quantitatively predicting thermally as well as optically measured trajectories is presented. Viewing dynamics of components as feedback interconnections [14], [21] together with system identification tools enable the modeling of complex processes by simpler components. Interconnections and simpler components provide useful insights into the overall dynamics. It is shown that all parameters used in the model can be identified using thermal-sensor output alone making this approach applicable where optical sensing is not available. The complex geometry of microelectromechanical system (MEMS) levers precludes a tractable physical model of thermal-sensor dynamics. It is shown that for practical operating amplitudes of dynamic-mode operation, linearized characterizations obtainable from black

Manuscript received February 10, 2009; revised October 14, 2009. First published December 22, 2009; current version published February 3, 2010. Subject Editor O. Tabata.

P. Agarwal and M. V. Salapaka are with the Department of Electrical and Computer Engineering, University Of Minnesota–Twin Cities, Minneapolis, MN 55455 USA (e-mail: agar0108@umn.edu; murtis@umn.edu).

D. R. Sahoo, A. Sebastian, and H. Pozidis are with the IBM Zürich Research Laboratory, 8803 Rüschlikon, Switzerland (e-mail: dsa@zurich.ibm.com; ase@zurich.ibm.com; hap@zurich.ibm.com).

Color versions of one or more of the figures in this paper are available online at <http://ieeexplore.ieee.org>.

Digital Object Identifier 10.1109/JMEMS.2009.2037340

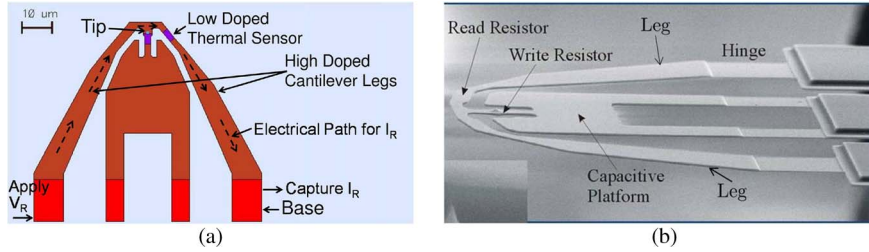


Fig. 1. (a) Schematic and (b) SEM image of the cantilever with integrated thermal sensor. The cantilever with integrated thermal sensor is made out of monolithic silicon. The legs are  $65 \mu\text{m}$  long and  $1.5 \mu\text{m}$  thick. Dimensions of the thermal sensor are  $4 \mu\text{m} \times 3.2 \mu\text{m} \times 0.5 \mu\text{m}$  ( $L \times W \times T$ ). The hinge is  $15 \mu\text{m}$  long and  $0.5 \mu\text{m}$  thick. The legs of the cantilever are doped higher at  $1\text{--}2 \times 10^{20} \text{ cm}^{-3}$  as compared with the thermal sensor which has a doping concentration of  $4 \times 10^{17} \text{ cm}^{-3}$ . The mass of the cantilever is roughly  $6 \times 10^{-13} \text{ kg}$ . There is a capacitive platform in the cantilever for electrostatic actuation. All the experiments in this study were done at room temperature with no active control of temperature, pressure, or humidity.

box identification techniques using Fourier methods suffice. It is discovered that the thermal-sensor output is affected by extraneous factors with capacitive and possibly magnetic origins that need to be considered. Experimental strategies that isolate these deleterious effects are presented. An experimental characterization of thermal-sensor dynamics is achieved and compared with finite-element method (FEM) simulations. The efficacy of the paradigm developed in this paper is verified with comparison between simulated and experimental data. In summary, this paper provides a comprehensive understanding of the physical effects governing the dynamics of an electrostatically actuated MEMS lever with integrated thermal sensing. It also provides a means of identifying time constants of various physical processes from thermal-sensor measurement. Steps needed to construct the model are straightforward, enabling quantitative real-time prediction of the motion of the cantilever and the thermal-sensor measurement.

## II. DEVICE DESCRIPTION AND MODELS

The cantilevers studied in this paper are made of highly doped material with a lowly doped region that forms the thermal sensor (see Fig. 1 and [22] for a detailed description). The resistance of the electrical path [see Fig. 1(a)] is primarily due to the resistance of the thermal sensor. The resistance of the rest of the electrical path is negligible. Thus, the current  $I_R$  flowing through the electrical path when a voltage  $V_R$  is applied is determined by the resistance of the thermal sensor. Thus, the heat dissipation in the thermal sensor results in a temperature change of the sensor. The proximity of the thermal sensor to the sample being imaged governs the heat lost from the cantilever to the substrate by conduction, and thereby, governs the temperature and resistance of the thermal sensor. As the sample is positioned laterally with respect to the cantilever, the distance between the sample and the thermal sensor is changed due to the topography of the sample. The lesser the distance between the cantilever and the sample, the more is the heat conducted from the cantilever to the sample. This leads to a reduction in the thermal-sensor temperature and an increase in the current. The aforementioned mechanism provides a means of inferring the topography of the substrate from the thermal-sensor output. In addition to the thermal sensor for measuring topography, an optical beam-bounce method is also employed to measure the cantilever deflection  $p$  that can form another sensor for topography measurement. In the experimental setup employed,

the sample can be moved with respect to the cantilever using piezoactuated scanners.

The cantilever is considered to be a flexure member and is modeled as a linear filter  $G$  (see Fig. 2).  $G$  processes the input forces on the cantilever and provides the displacement  $p$  of the cantilever as the output. The main forces on the cantilever are externally induced electrostatic forces  $F_{\text{esf}}$  and the tip-sample interaction forces  $F_{\text{ts}}$ . The tip-sample interaction forces are appreciable over a relatively shorter range when compared with electrostatic forces. Tip-sample interaction forces, which include Van der Waals, adhesive, and meniscus forces, are negligible for tip-sample separation  $t_s$  that is greater than  $2 \text{ nm}$ , whereas the electrostatic force remains effective over the entire operating range of the cantilever motion. Electrostatic forces are realized by applying a voltage  $V_{\text{sub}}$  to the substrate.

The tip-sample interaction forces bear a complex relationship, particularly for dynamic-mode operation, to the cantilever dynamics  $G$ . The tip-sample interaction forces depend on the tip-deflection  $p$  and are modeled by the relation  $F_{\text{ts}}/m = \Phi(t_s)$ , where  $\Phi$  is a nonlinear map that has the qualitative features of a Lennard Jones potential and  $m$  is the “mass” of the cantilever. However, the deflection  $p$  depends on tip-sample interaction forces. This interdependence is modeled by a feedback interconnection of  $G$  and  $\Phi$ . Fig. 2 shows such an interconnection where  $p$  and  $z_s$  denote cantilever position and sample height, respectively, with the tip-sample separation given by  $t_s = p - z_s - t_h + \ell_0$  (see Fig. 3 for notations).

A piecewise linear model is assumed to approximate the tip-sample interaction force described by

$$\begin{aligned} F_{\text{ts}} &= 0, & \text{if } t_s > d \\ &= k_a(t_s - d), & \text{if } 0 \leq t_s \leq d \\ &= k_r t_s + k_a(t_s - d), & \text{if } t_s \leq 0 \end{aligned} \quad (1)$$

where  $t_s$  is the tip-sample separation,  $d$  is a parameter that characterizes the onset of the attractive interaction,  $k_a$  is the spring constant modeling attractive tip-sample interaction forces and  $k_r$  is the spring constant modeling repulsive forces [21]. The origin is placed at the onset of the repulsive interaction. This model depends on the parameters  $k_r$ ,  $k_a$ , and  $d$ . Effects of adhesive and meniscus forces are accounted for by suitably modifying parameters  $d$  and  $k_a$ .

When the voltage  $V_R$  is applied across the legs of the cantilever and  $V_{\text{sub}}$  is applied to the sample that can be assumed

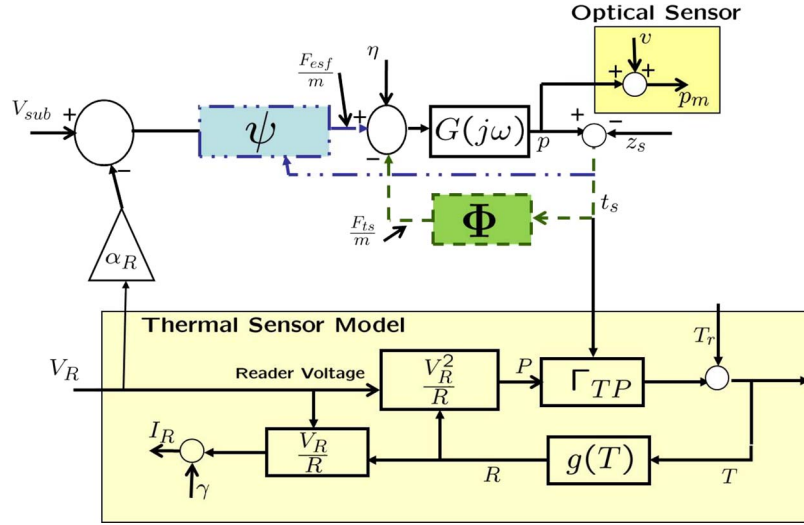


Fig. 2. Integrated systems model with a detailed model of the thermal sensing mechanism. The cantilever beam is modeled as a second-order linear time-invariant system  $G(j\omega)$  which takes as input the thermal noise force  $\eta$ , electrostatic force (per unit mass)  $F_{\text{esf}}$  and tip-sample interaction force (per unit mass)  $F_{\text{ts}}$  and gives tip deflection  $p$  as the output.  $p$  is measured by an optical sensor where the output is  $p_m$  and is corrupted by a measurement noise  $\nu$ . Electrostatic force  $F_{\text{esf}}$  depends on the instantaneous potential difference between the cantilever and the sample which is modeled as  $\alpha_R V_R - V_{\text{sub}}$ .  $\alpha_R$  accounts for the nonuniform potential distribution along the cantilever legs. Tip-sample separation  $t_s = p - z_s$  modulo  $(\ell_0 - t_h)$  is sensed by a thermal sensor which takes as input the tip-sample separation  $t_s$  and the thermal-sensor voltage  $V_R$ , and gives current  $I_R = V_R/R$  as the output. Measurement of  $I_R$  is corrupted by measurement noise  $\gamma$ .  $\Gamma_{TP}$  is the dynamic map that relates instantaneous power dissipation ( $V_R^2/R$ ) in the cantilever and instantaneous tip-sample separation ( $t_s$ ) to the cantilever temperature ( $T$ ). Resistance  $R$  of the thermal sensor is related to temperature ( $T$ ) by a nonlinear static map  $g(T)$ .

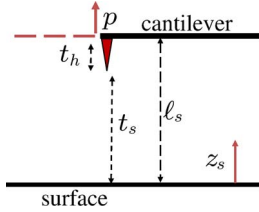


Fig. 3.  $p$  and  $z_s$  are the tip-deflection and the sample position, respectively.  $t_s$  and  $t_h$  are the tip-sample separation and the tip height, respectively.  $\ell_0$  can be interpreted as the initial reference distance between the sample and a nominal point on the lever surface. The lever-sample separation  $\ell_s$  is the instantaneous separation between the cantilever and the sample.

uniform across the substrate, the voltage difference between the cantilever and the sample varies with the spatial coordinate on the cantilever surface. This variation is caused due to the variability of the resistance along the cantilever. The cantilever surface and the substrate are modeled as a parallel-plate capacitor with the voltage difference being

$$V_{\text{esf}} = \alpha_R V_R - V_{\text{sub}} \quad (2)$$

where  $\alpha_R$  is the scaling factor that accounts for the nonuniform voltage on the cantilever surface. The capacitive (electrostatic) force on the cantilever is described by

$$\begin{aligned} F_{\text{esf}} &= -\frac{K_{\text{esf}} V_{\text{esf}}^2}{\ell_s^2}, \quad \text{if } \ell_s > t_h \\ &= -\frac{K_{\text{esf}} V_{\text{esf}}^2}{t_h^2}, \quad \text{if } \ell_s \leq t_h \end{aligned} \quad (3)$$

where  $V_{\text{esf}}$  is given by (2),  $K_{\text{esf}}$  is an electrostatic force constant, and  $\ell_s = \ell_0 + p - z_s$  is the instantaneous lever-sample separation. The aforementioned characterization reflects the fact that if the lever-sample distance  $\ell_s$  is smaller than the tip-

height  $t_h$  then  $t_h$  governs the electrostatic force on the cantilever. The aforementioned model depends on parameters  $K_{\text{esf}}$ ,  $\ell_0$ ,  $t_h$ , and  $\alpha_R$ . Similar to the tip-sample interaction force, the cantilever deflection affects the electrostatic force, which, in turn, is affected by the electrostatic force. This scenario admits a feedback interconnection as shown in Fig. 2 (dashed-dot line). One crucial difference between the electrostatic and tip-sample forces is that the electrostatic forces, although nonlinear, admit a more precise physical model. Unlike tip-sample interaction forces, (that are, in a sense, to be measured) electrostatic forces are introduced in a controlled manner. Fig. 2 also shows the assumption that electrostatic and tip-sample forces appear additively on the cantilever. Measurement of cantilever deflection  $p$  is corrupted by white noise  $\nu$  with a variance of 100 pm and the measurement of the thermal-sensor output  $I_R$  is corrupted by white noise  $\gamma$  with a variance of 107  $\mu\text{A}$ .

#### A. Thermal-Sensor Model

A voltage  $V_R$  generates a current  $I_R = V_R/R$  through the cantilever depending on the instantaneous resistance  $R$  of the cantilever. The generated heat in the thermal sensor, with power  $P = V_R^2/R$ , dissipates by conduction through the cantilever legs as well as to the sample through the surrounding medium. The operator  $\Gamma_{TP}$  (see Fig. 2) maps the dissipated power to the thermal-sensor temperature  $T$ . It is assumed that time constants relating the resistance and the temperature of the thermal sensor are negligibly small. It is thus assumed that a relation  $R = g(T)$  holds, with  $g$  being a static, nonlinear, and memoryless map. Thermal-sensor dynamics is also cast as a feedback interconnection (see Fig. 2) wherein the dissipated power leads to a temperature change of the sensor, which leads to a change in the sensor resistance, which, in turn, changes the power dissipated in the thermal sensor. Such a model was



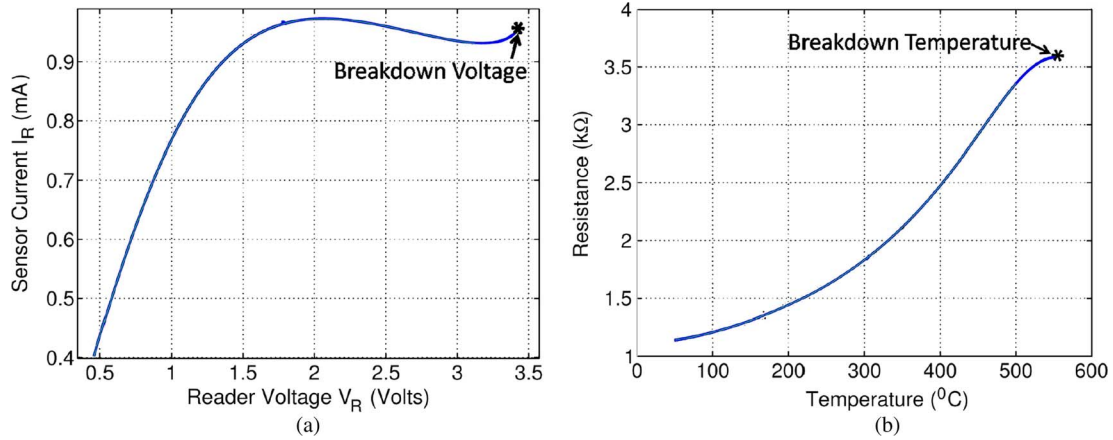


Fig. 4. (a) Experimentally obtained  $I$ - $V$  curve. Voltage  $V_R$  is ramped up linearly from 0 to 3.5 V and then ramped down linearly at 3 Hz. Thermal-sensor output  $I_R$  is measured. This is done in a quasi-static manner so that at each point, the thermal sensor is in equilibrium with its surroundings. Breakdown voltage is  $\approx 3.4$  V. (b) Experimentally identified nonlinear static relationship  $g(T)$  between thermal-sensor resistance ( $R$ ) and temperature ( $T$ ). This relationship is assumed to be the same for all the operating points of  $V_R$  and  $t_s$ .

first developed in [14] to shape the temperature profile of the write heater for the contact-mode operation. In this paper, the sensing dynamics of the read heater (thermal sensor that is used to read bits in a high-density data-storage application) for dynamic-mode operation is addressed. As the power dissipation depends on the applied voltage  $V_R$  and tip-sample distance  $t_s$ , it follows that  $\Gamma_{TP} = \Gamma_{TP}(V_R, t_s)$ . The aforementioned description requires characterization of  $\Gamma_{TP}$  and  $R = g(T)$ . Unlike the models for the forces presented earlier, an exact form of the operator  $\Gamma_{TP}$  is not known for realistic cantilever geometries, even though some intuition of the form of the  $\Gamma_{TP}$  operator is gained from closed-form expressions derived for simplified cantilever geometries [13].

### III. SYSTEM IDENTIFICATION

The characterization framework provided in the previous section assumes the following: 1) that the cantilever and the substrate form a parallel-plate capacitor. Even though the sample remains flat, bending of the cantilever due to forces might violate these assumptions; 2) that adhesive, meniscus, and tip-sample interaction forces appear as single piecewise linear forces; and 3) that the cantilever mechanical response is in cascade with the thermal-sensor dynamics. Typically, the temperature  $T(x, t)$  is a function of position ( $x$ ) along the legs and time. Thus, the operator  $\Gamma_{TP}$  that maps the thermal-sensor voltage  $V_R$  and the tip-sample separation  $t_s$  to thermal-sensor temperature  $T$  is also dependent on  $x$ . In this paper, we assume a lumped parameter model wherein  $T$ , which is not a function of  $x$ , is able to predict changes in the thermal-sensor current  $I_R$ . This makes the operator  $\Gamma_{TP}$  independent of  $x$ . As will be demonstrated later, these assumptions are realistic, and, furthermore, an effective means of identifying parameters from experimental data will be developed. As optical sensing is not available in many integrated applications, it will be shown that the model parameters can be identified accurately using only thermal-sensor measurement and electrostatic actuation. The optical deflection signal will be used to verify the accuracy of identified parameters and understand the dynamics of the cantilever beam.

#### A. Thermal-Sensor-Based Identification

In this section, the aim is to estimate all physical parameters of the system shown in Fig. 2, from thermal-sensor measurement alone, and to compare the estimates with the ones obtained from the optical signal.

1) *I-V Curves and Resistance as a Function of Temperature:* In this part, we provide a method to identify  $g(T)$ . The input  $V_R$  is first ramped up and then ramped down in a quasi-static manner at 3 Hz, and the signal  $I_R$  is recorded [see Figs. 2 and 4(a)]. Since the current and the applied voltage  $V_R$  are known, the resistance  $R = V_R/I_R$  can be found. Similarly, once  $R$  is known, the power  $V_R^2/R$  can be evaluated. As the power  $P$  or the current through the thermal sensor is increased beyond a value  $P_k$ , the characteristics of the sensor change abruptly due to intrinsic carrier thermal runaway [17], [18]. The thermal sensor in this study is n-doped using phosphorous with a doping concentration of approximately  $4 \times 10^{17} \text{ cm}^{-3}$ . The temperature  $T_k$  at which this breakdown of the sensor happens depends on the doping concentration of the heater and is calculated to be  $550^\circ\text{C}$  [13]. The power  $P_k$  at which the breakdown happens can be read from the data by recognizing the “knee” in the  $P$ - $V_R$  relationship [23]. Note that the temperature at the thermal sensor is  $T_r$  (the room temperature) when the power is zero. From the aforementioned identification, the pair  $(T_k, P_k)$  is known. In the aforementioned experiment where  $V_R$  is ramped up and down, the ramp input is slow. Therefore, from the linearity assumption of the power-temperature map  $\Gamma_{TP}$ , at a particular tip-sample separation, it follows that the slope of the line joining  $(T_r, 0)$  and  $(T_k, P_k)$  identifies  $K_{TP}$ , the dc gain of  $\Gamma_{TP}$ , using the relationship  $K_{TP} = (T_k - T_r)/(P_k - 0)$ . Once this information is obtained, the temperature  $T$  can be found at various values of  $V_R$  using the relationship  $T = K_{TP}P + T_r$ . The resistance at the corresponding values of  $V_R$  was found earlier, and, thus, the functional dependence  $g(T)$  of the resistance  $R$  on temperature  $T$  [see Fig. 4(b)] can be found.

2) *Relationship of Power-Temperature DC Gain  $K_{TP}$  Versus Tip-Sample Separation  $t_s$ :* The relationship between the power-temperature dc gain  $K_{TP}$  and tip-sample separation  $t_s$  can be found by keeping  $V_R$  constant and performing a force

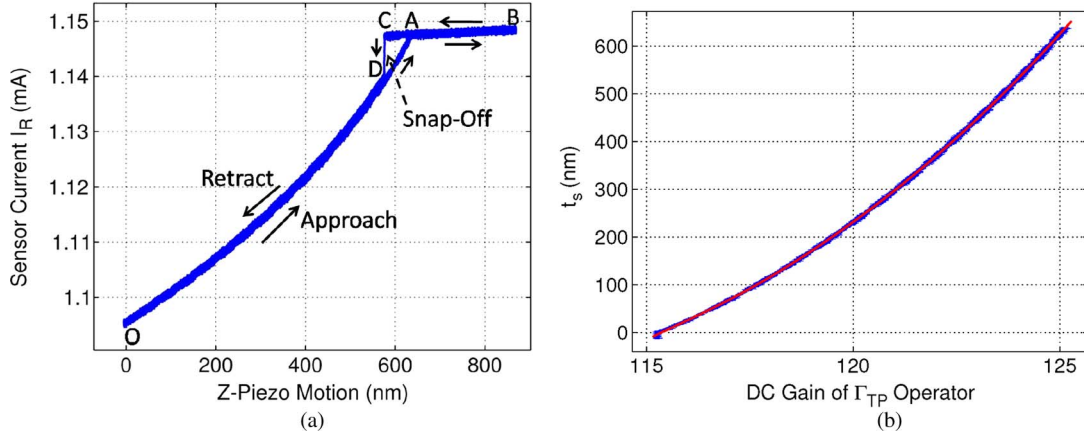


Fig. 5. (a) Experimental  $z$  force curve with the monitored signal being  $I_R$ .  $z$ -piezo is ramped up linearly by a distance of 900 nm and then ramped down at 3 Hz. Thermal-sensor output  $I_R$  is recorded. The piezo is ramped up from O to A to B. At A, the tip comes into contact with the sample. The piezo is then ramped down from B to C to D to O. At C, the tip loses its contact with the sample. This is called snap-off. (b) Experimentally obtained dc gain of  $\Gamma_{TP} = K_{TP}$  as a function of  $t_s$  is plotted.  $K_{TP}$  is a strong function of  $t_s$  which results in tip-sample separation sensing capability of the thermal sensor.

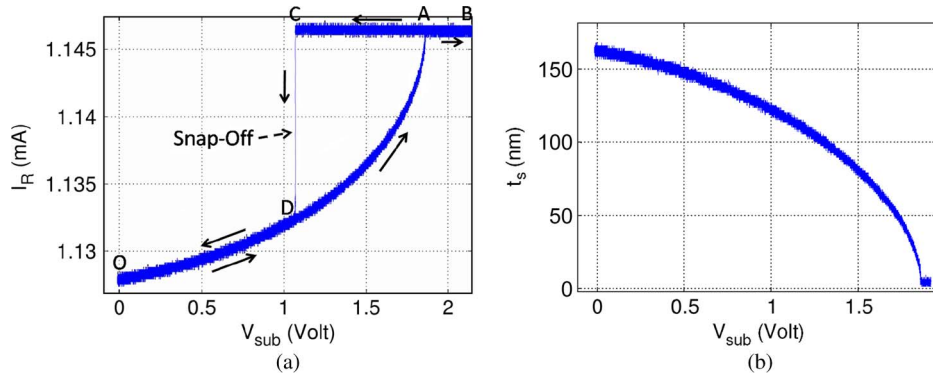


Fig. 6. (a) Experimental electrostatic force curve with no snap-in, i.e., the cantilever tip is in stable equilibrium with the forces at all the points in electrostatic force curve.  $V_{sub}$  is ramped up from O to A to B. At A, the tip comes into contact with the sample. The piezo is then ramped down from B to C to D to O. At C, the tip snaps-off the sample. (b) The  $I_R$  axis in (a) converted to the tip-sample separation  $t_s$  axis. This experiment is performed to check the validity of the assumptions made in converting the  $I_R$  axis to the  $t_s$  axis. The flat portion ( $t_s$  not changing with  $V_{sub}$ ) should be at a value of  $t_s = 0$ . The small experimental value indicates that the assumptions made during conversion of  $z_s$  into  $t_s$  are reasonably valid.

curve with the sample position  $z_s$  as the input and  $I_R$  as the output. Such a force curve is shown in Fig. 5(a) where the tip-sample separation is reduced linearly and then increased linearly by applying a triangle wave at the  $z$ -piezo.

During the force-curve experiments, where the input is a ramp applied to the  $z$ -piezo or  $V_{sub}$ , the restoring spring force on the cantilever is balanced by tip-sample interaction force or attractive electrostatic force, respectively, at each point. A scenario can occur where the tip-sample interaction force or the electrostatic force is no longer balanced by the restoring spring force resulting in instability. This causes the tip to crash into the sample. Such a scenario is called “snap-in.” For electrostatic force curve, snap-in condition can be controlled by controlling the initial tip-sample separation. It can be avoided by reducing the initial tip-sample separation. When the tip is in contact with the sample and the tip-sample separation is being increased, then the tip sticks to the sample for an extended time due to the adhesive and meniscus forces. It then releases suddenly. This scenario is called “snap-off.”

Note that for a given  $V_R$  and  $z_s$ , as  $I_R$  is known,  $R = V_R/I_R$  can be evaluated, and thus,  $P = V_R^2/R$  can be found. Moreover, as  $g(T)$  and  $g^{-1}(R)$  are functions that were evaluated

previously, the temperature can be found by  $T = g^{-1}(R) - T_r$ . Thus, the ratio  $K_{TP} = P/T$  can be found at each value of  $z_s$ . The task of converting  $z_s$  to tip-sample separation remains. It is assumed that the value  $z_{sn}$  of  $z_s$  at which the tip snaps into contact with the sample in the  $I_R - z_s$  force curve is where the tip-sample separation is zero. Cantilever bending is assumed to be negligible during  $z$  force curve when the tip is not in contact with the sample. With these assumptions, the sample position  $z_s$  can be converted to  $t_s$  as  $t_s = z_{sn} - z_s$ . As  $K_{TP}$  is known at each value of  $z_s$ , the plot of  $K_{TP}$  versus  $t_s$  can be obtained [see Fig. 5(b)].

The validity of the assumptions to obtain  $K_{TP}$  versus  $t_s$  relationship is assessed by performing an electrostatic force curve where  $V_{sub}$  is ramped up and down at 3 Hz, and  $I_R$  is recorded [see Fig. 6(a)].  $V_R$  is chosen to prevent the tip from snapping into contact with the sample ([24]).  $I_R$  can be converted to  $t_s$  by the following steps:  $R = V_R/I_R$ ,  $P = V_R^2/R$ ,  $T = g^{-1}(R) - T_r$ , and  $K_{TP} = P/T$ . Once  $K_{TP}$  is known, using Fig. 5(b),  $t_s$  can be evaluated. Thus, the  $I_R - V_{sub}$  plot is converted to  $t_s - V_{sub}$  plot [see Fig. 6(b)]. Note that when  $t_s = 0$ , any further change in  $V_{sub}$  cannot change the current  $I_R$ . Thus, the value of  $t_s$  where the  $I_R$  remains constant (the part

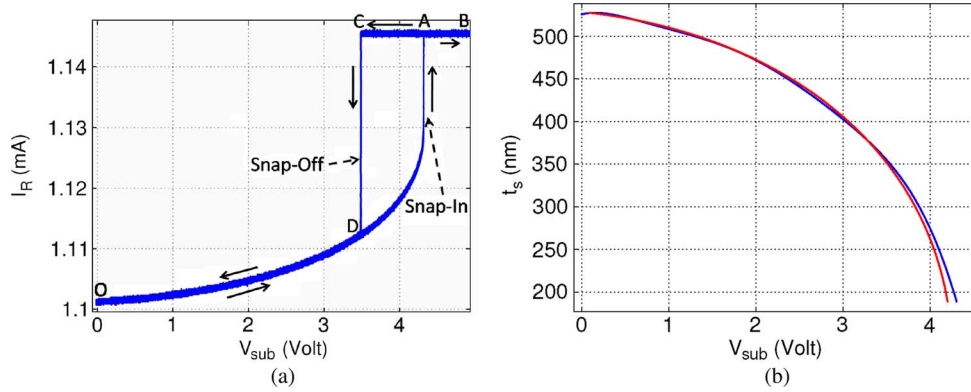


Fig. 7. (a) Experimental electrostatic force curve with  $I_R$  versus  $V_{sub}$  plotted.  $V_{sub}$  is ramped up from O to A to B. At A, the tip comes into contact with the sample suddenly. This is called snap-in. The piezo is then ramped down from B to C to D to O. At C, the tip snaps-off the sample. The  $I_R$  axis is converted to the tip-sample separation axis; a polynomial fit is obtained to obtain a clean version of the data. The region where the tip-sample interaction forces are negligible is used to identify the model parameters. (b) (Red-dashed) The parameter fit and (blue-solid) experimental data. The estimated model compares well with the experimental data at large tip-sample separation. Slight deviation is observed at small tip-sample separation indicating that the parallel-plate model for electrostatic force is not sufficient to capture the cantilever behavior in this region.

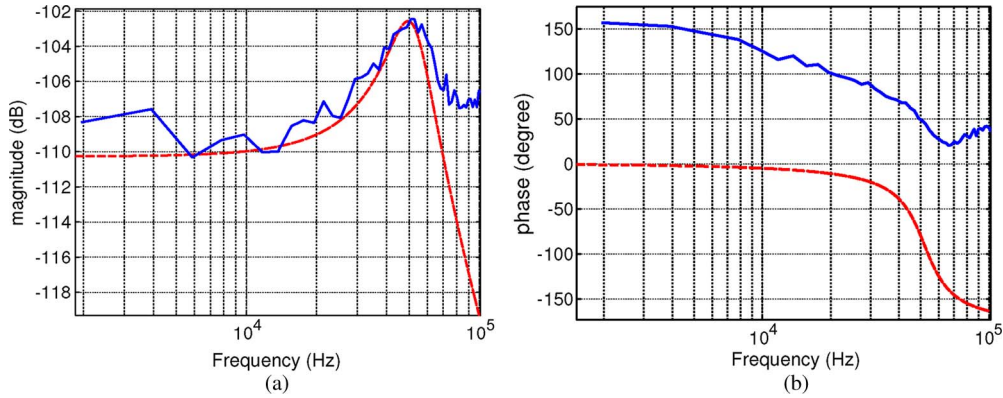


Fig. 8. Fitting a second-order transfer function around the resonance in the measured transfer function from  $V_{sub}$  to  $I_R$ . (a) Magnitude. (b) Phase. Blue solid line is the experimentally obtained response of  $\Gamma_{I_R \tilde{V}_{sub}}$  and red dashed line is the second-order fit around resonance. This process allows estimation of  $f_0$  and  $Q$  of the cantilever from the thermally sensed data.

of the curve in Fig. 6(b) that remains constant) should be zero. This value is approximately 5.8% of the entire trajectory. This discrepancy, although small, is attributed to partial violation of the assumptions which were made during the conversion of  $z_s$  into  $t_s$ .

3) *Electrostatic Force Curve for Identification*: Consider an electrostatic force curve with  $V_{sub}$  as input and  $I_R$  as the monitored variable where the tip does snap into contact with the sample [see Fig. 7(a)]. By converting  $I_R$  to  $t_s$ , the  $t_s$  versus  $V_{sub}$  plot, as shown in Fig. 7(b), is obtained.

In the region of the force curve where the tip-sample interaction forces are negligible, forces on the cantilever are predominantly electrostatic, and the equilibrium position  $p = t_s + t_h - \ell_0$  of the cantilever satisfies

$$k(t_s + t_h - \ell_0)(t_s + t_h)^2 = -K_{esf}(-V_{sub} + \alpha_R V_R)^2. \quad (4)$$

The previous equation is a polynomial in data  $(t_s, V_{sub})$  where the coefficients  $k$ ,  $t_h$ ,  $\ell_0$ ,  $K_{esf}$ , and  $\alpha_R$  have nonlinear dependence on each other. Nonlinear least-square curve-fitting algorithm [25] is used to identify the best fit to the data in Fig. 7(b). Parameters identified are  $\alpha_R$ ,  $K_{esf}$ ,  $k$ ,  $t_h$ , and  $\ell_0$ , where  $k$  is the cantilever spring constant.

The estimation of mechanical cantilever parameters, viz., the resonant frequency and quality factor of  $G(j\omega)$ , is done by fitting a second-order transfer function around the resonance of the transfer function from  $V_{sub}$  to  $I_R$  (see Fig. 8). Experimental data for this step are collected at a large tip-sample separation such that the electrostatic force does not alter the parameters of the cantilever mechanical response  $G(j\omega)$  significantly. This provides an estimate of  $f_0$  as 51.8578 kHz and the quality factor  $Q$  as 2.37148. Estimating the relationship of the cantilever deflection  $p$  and the electrostatic force using only the thermal-sensor measurement involves decoupling the thermal-sensor dynamics from the mechanical dynamics of the cantilever. An optical beam-bounce method provides a direct measure of  $p$  without introducing its own dynamics and therefore provides precise characterization of the relationship between  $V_{sub}$  and  $p$ . The  $p$ - $V_{sub}$  relationship as obtained independently from the optical beam-bounce measurement and from the thermal-sensor measurement, respectively, is shown in Fig. 9. Evidently, with the methods provided, there is a quantitative match of the thermal-sensor-based model response to the optical beam-bounce-based experimentally measured response, indicating that  $G(j\omega)$  can be identified well from thermal-sensor data alone.



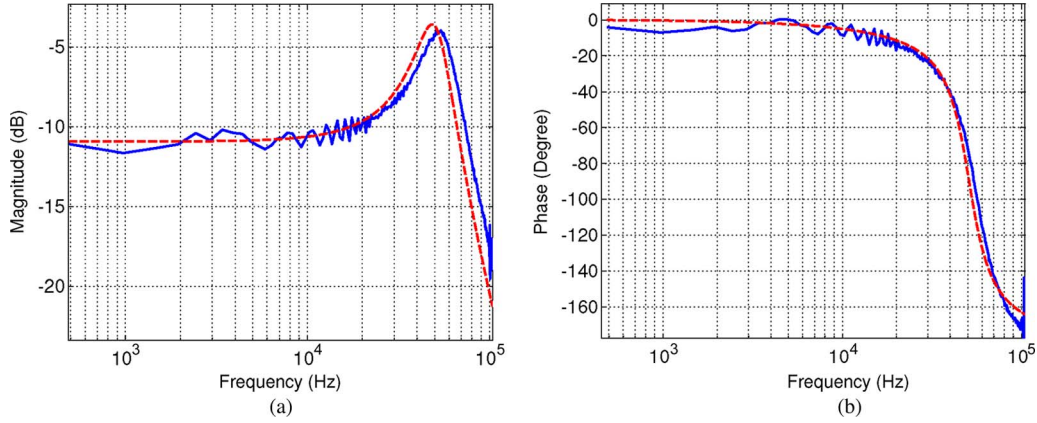


Fig. 9. Cantilever mechanical transfer function  $G(j\omega)$ . (a) Magnitude comparison (b) Phase comparison. Blue-solid line is experimental cantilever mechanical transfer function obtained using optical beam-bounce method. Red-dashed line is second-order fit around the resonance of the  $\Gamma_{\tilde{I}_R \tilde{V}_{sub}}$  transfer function obtained using thermal-sensor output  $\tilde{I}_R$  (see Fig. 8). Good agreement between both the plots indicate that parameters for the cantilever mechanical transfer function can be estimated from the thermal-sensor output alone in the absence of an optical sensor.

TABLE I  
COMPARISON OF THE OPTICAL-SENSOR- AND  
THERMAL-SENSOR-BASED IDENTIFIED  
PARAMETER VALUES

Parameter	Optical	Thermal
$\alpha_R$	0.2504	0.2156
$\ell_0$	1166 nm	1243 nm
$K_{esf}$	1.39744e-021	1.64991e-21
$t_h$	not estimated	711.75 nm
$k$	0.14123	0.13975
$f_0$	54.41 kHz	51.858 kHz
$Q$	2.1234	2.3715

Thus, using the aforementioned procedure, model parameters can be estimated fairly well using the thermal-sensor output and actuation signal  $V_{sub}$ .

### B. Virtual Position Sensor

The cantilever, the tip-sample interaction, and the electrostatic interaction models can be identified based on the optical beam-bounce measurement of the cantilever deflection  $p$ . The optical measurement does not introduce any new dynamics unlike the thermal sensor and, therefore, is expected to provide a more precise and easier identification of parameters. Such an identification strategy is reported in [23], which also demonstrates that optical sensor-based identified parameters quantitatively predict cantilever deflection. Table I provides a comparison of the parameters as identified by the thermal sensor using the methods proposed earlier in this paper and the optical-sensor-based methods. The fact that these models are amenable to real-time implementation and fast simulations facilitate better understanding of the device, and obviate the need for elaborate experiments to test various hypotheses. In an integrated environment, where optical position sensing is not available, the proposed technique enables estimation of parameters from thermal-sensor measurement. One can then obtain estimates of cantilever position in real time from the implementation of this model. This can be viewed as a virtual position sensor that replaces the optical sensor.

## IV. DYNAMIC CHARACTERIZATION OF THERMAL SENSOR

In this section, the notation  $\Gamma_{oi}$  will denote the dynamic operator between the input  $i$  and output  $o$ . Thermal means of sensing topography enables an operation where an array of cantilevers can probe the sample in a parallel operation. However, the thermal sensor introduces new dynamics (unlike the optical beam-bounce method) that need to be understood for appropriate interpretation of data. In addition, there are a number of applications where the thermal sensor is used to study thermal processes at the nanoscale. A dynamic characterization of the thermal sensor provides insights on how to better employ these sensors for fundamental studies of thermal transport and also characterizes the limitations and capabilities of the sensor. In this section, the primary aim is to understand thermal-sensor dynamics and its relation to cantilever dynamics. Note that, in the previous sections, a quasi-static characterization of the thermal sensor was achieved.

Unlike the electrostatic-force model where the form of forcing is known (3), physical models relating the dissipated power to the temperature of the thermal sensor for realistic cantilever geometries are not readily available for the operator  $\Gamma_{TP}$ . A characterization of the operator for quasi-static inputs is achieved in Section III at different tip-sample separations [see Fig. 3(b)].  $\Gamma_{TP}$  operator can be linearized (see Fig. 10) about a nominal operating point,  $(V_{R0}, t_{s0})$ , as follows:

$$\Delta T = \underbrace{\frac{\partial \Gamma_{TP}}{\partial P} \bigg|_{P_0, t_{s0}}}_{C(j\omega)} \Delta P + \underbrace{\frac{\partial \Gamma_{TP}}{\partial t_s} \bigg|_{P_0, t_{s0}}}_{H(j\omega)} \Delta t_s. \quad (5)$$

where  $C(j\omega)$  characterizes the linear relationship between small changes in power dissipation  $\Delta P$  and small changes in the thermal-sensor temperature  $\Delta T$ , and  $H(j\omega)$  captures the linear relationship between small changes in the tip-sample separation  $\Delta t_s$  and the small changes in thermal-sensor temperature  $\Delta T$  at a particular operating point  $(V_{R0}, t_{s0})$ . It is assumed that the temperature of the thermal sensor depends primarily on the power  $P$  and the tip-sample separation  $t_s$ .

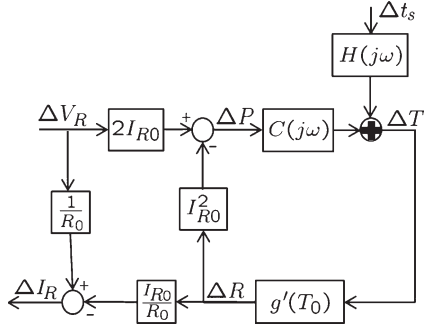


Fig. 10. Small signal model for the thermal sensor about a nominal point  $(I_{R0}, R_0, T_0)$ .  $\Gamma_{TP}$  has been linearized as in (5).  $C(j\omega)$  is the frequency response from  $\Delta P$  to  $\Delta T$ , and  $H(j\omega)$  is the frequency response from  $\Delta t_s$  to  $\Delta T$ . Nonlinear operators  $V^2/R$ ,  $V/R$ , and  $g(T)$  are also linearized to obtain the rest of the model.

As no physical model to describe the dynamics of the operator  $\Gamma_{TP}$  is available, the validity of the small signal model in (5) takes special significance. If the small signal model is valid for practical operating conditions of dynamic mode, then one can identify the small signal model parameters in (5) using Fourier methods. One can thus overcome the lack of a tractable physical model of the operator  $\Gamma_{TP}$ . Fortunately, as is shown later in this paper, a small signal model does suffice for quantitative prediction of the thermal trajectories in the dynamic mode.

Nonlinear operators  $V_R/R$ ,  $V_R^2/R$ , and  $R = g(T)$  (see Fig. 2) can also be linearized about the operating point  $(I_0, R_0, T_0, P_0, t_{s0}, V_{R0})$  to obtain a small signal model for the thermal sensor (see Fig. 10). The dynamic relationships  $\Gamma_{\tilde{I}_R \tilde{t}_s}$  (sensing transfer function) and  $\Gamma_{\tilde{I}_R \tilde{V}_R}$  (thermal transfer function) that relate tip-sample separation to thermal-sensor current and  $V_R$  to thermal-sensor current, respectively, can be experimentally obtained by varying  $V_R$  and  $t_s$  while measuring  $I_R$  (the means of varying  $t_s$  are discussed later). Note that the sensing transfer function is of fundamental importance as it provides information on the speed with which the thermal sensor can measure the topography of the sample.

Using the small signal model shown in Fig. 10, the following relationships can be derived:

$$\Gamma_{\tilde{I}_R \tilde{V}_R} = \frac{\Delta I_R}{\Delta V_R} = \frac{1}{R_0} \left[ \frac{1 - g'(T_0)C(j\omega)I_{R0}^2}{1 + g'(T_0)C(j\omega)I_{R0}^2} \right] \quad (6)$$

$$\Gamma_{\tilde{I}_R \tilde{t}_s} = \frac{\Delta I_R}{\Delta t_s} = \frac{-I_{R0}}{R_0} \left[ \frac{g'(T_0)H(j\omega)}{1 + g'(T_0)C(j\omega)I_{R0}^2} \right]. \quad (7)$$

From (6), it follows that

$$C(j\omega) = \frac{1}{I_{R0}^2 g'(T_0)} \left[ \frac{1 - R_0 \Gamma_{\tilde{I}_R \tilde{V}_R}}{1 + R_0 \Gamma_{\tilde{I}_R \tilde{V}_R}} \right]. \quad (8)$$

Note that from (7) and (8), it follows that

$$H(j\omega) = \frac{-R_0}{I_{R0} g'(T_0)} \Gamma_{\tilde{I}_R \tilde{t}_s} \left[ \frac{2}{1 + R_0 \Gamma_{\tilde{I}_R \tilde{V}_R}} \right]. \quad (9)$$

Such a relationship as (8) provides useful information on the rate at which the thermal sensor can be heated and therefore translates into assessing, for example, the write speeds in a

high-density data-storage application. Once  $C(j\omega)$  and  $H(j\omega)$  are identified, important closed-loop relations (for example,  $\Delta V_R$  to  $\Delta T$ ) can be obtained, which reflect on the bandwidth with which the temperature of the thermal sensor can be changed using voltage  $V_R$ . Since a direct measurement of  $\Delta T$  is not available,  $\Gamma_{\tilde{I}_R \tilde{V}_R}$  and  $\Gamma_{\tilde{I}_R \tilde{t}_s}$  are first obtained experimentally.  $C(j\omega)$  and  $H(j\omega)$  are then evaluated using (8) and (9).

Electrostatic forcing of the cantilever changes the tip-sample separation  $t_s$ , allowing  $\Gamma_{\tilde{I}_R \tilde{t}_s}$  to be obtained. The small signal model  $\Gamma_{\tilde{t}_s \tilde{V}_{\text{esf}}}$  that relates small changes in  $V_{\text{esf}}$  to small changes in tip-sample separation  $t_s$  can be found by linearizing the nonlinear electrostatic forcing (3), as follows:

$$\underbrace{\ddot{p} + \frac{\omega_0}{Q_0} \dot{p} + \omega_0^2 p}_{G(j\omega) \text{ dynamics}} = \omega_0^2 \left( \frac{-K_{\text{esf}} V_{\text{esf}}^2}{(l_0 + p)^2} \right)$$

$$\ddot{p} + \frac{\omega_0}{Q_0} \dot{p} + \omega_0^2 p = \omega_0^2 \left( \frac{-2K_{\text{esf}} V_{\text{esf}0}}{(l_0 + p_0)^2} \Delta V_{\text{esf}} + \frac{2K_{\text{esf}} V_{\text{esf}0}^2}{(l_0 + p_0)^3} \Delta p \right).$$

Thus, the following relationships can be evaluated (see Fig. 2) and are found to be:

$$\Gamma_{\tilde{p} \tilde{V}_{\text{esf}}} = L \frac{\omega'^2}{s^2 + \frac{\omega'}{Q'} + \omega'^2}$$

$$\omega' = \omega_0 \sqrt{1 - \frac{2K_{\text{esf}} V_{\text{esf}0}^2}{(l_0 + p_0)^3}}$$

$$Q' = Q_0 \sqrt{1 - \frac{2K_{\text{esf}} V_{\text{esf}0}^2}{(l_0 + p_0)^3}}$$

$$L = \frac{-2K_{\text{esf}} V_{\text{esf}0}}{(l_0 + p_0)^2} \left[ 1 - \frac{2K_{\text{esf}} V_{\text{esf}0}^2}{(l_0 + p_0)^3} \right]^{-1} \quad (10)$$

where  $V_{\text{esf}0}$  and  $p_0$  are nominal electrostatic voltage and cantilever deflection, respectively, and it is assumed that the sample height is not varying.

*Remark:* It is evident from (10) that  $Q'$  and  $\omega'$  reduce as the lever-sample separation  $(l_0 + p_0)$  reduces. The dc gain  $L$  of frequency response  $\Gamma_{\tilde{p} \tilde{V}_{\text{esf}}}$  increases as the lever-sample separation decreases. Experimental results confirm these trends, as shown in Fig. 11. As the tip-sample separation increases,  $Q'$  and  $\omega'$  converge to  $Q_0$  and  $\omega_0$ , the latter being the cantilever model parameters without electrostatic forcing.  $L$  converges to zero indicating that the effect of electrostatic forcing reduces with increasing tip-sample separation. Cantilever parameter identification is therefore done at a tip-sample separation, where  $Q'$  and  $\omega'$  are close to  $Q_0$  and  $\omega_0$ , and  $L$  is sufficient to actuate the cantilever.

$\Gamma_{\tilde{t}_s \tilde{V}_{\text{esf}}}$ ,  $\Gamma_{\tilde{I}_R \tilde{t}_s}$  and  $\Gamma_{\tilde{I}_R \tilde{V}_R}$  can be represented as in Fig. 12 where it is assumed that the cantilever sensor with  $V_{\text{esf}}$  as an input and  $I_R$  as the output can be modeled as a cascade in series of two maps: the mechanical transfer function that maps the substrate voltage  $V_{\text{sub}}$  to the tip deflection  $p$  and the thermal



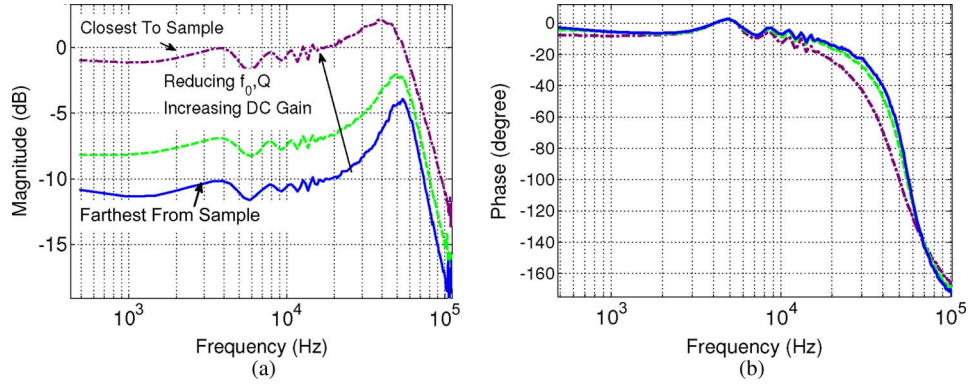


Fig. 11. Experimentally obtained (a) magnitude and (b) phase of the cantilever mechanical transfer function ( $V_{\text{sub}}$  to  $p$ ) at various tip-sample separation. The tip-sample separation increases from top to bottom. DC gain increases with reducing tip-sample separation, and  $f_0$  and quality factor  $Q$  decrease with reducing tip-sample separation as indicated by (10).

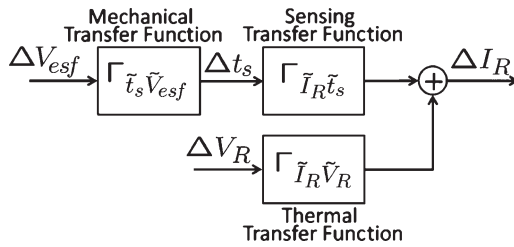


Fig. 12. Simulation model for an electrostatically actuated cantilever with integrated thermal sensor, about a nominal point of operation of dynamic-mode operation. Tip-sample separation  $t_s$  changes in response to changes in the electrostatic voltage  $V_{\text{esf}}$  related by transfer function  $\Gamma_{\tilde{t}_s \tilde{V}_{\text{esf}}}$ . Any change of sample profile  $z_s$  in the cantilever trajectory manifests itself in  $\Delta t_s$ .  $\Delta t_s$  perturbs the thermal system and results in a consequent change in the thermal-sensor output  $I_R$  related by the transfer function  $\Gamma_{\tilde{I}_R \tilde{t}_s}$ . This map is low-pass in nature with a bandwidth of approximately 12 kHz (see Fig. 16). Alternatively,  $\Delta I_R$  can also change through  $\Delta V_R$  related by the transfer function  $\Gamma_{\tilde{I}_R \tilde{V}_R}$ . All these three maps are experimentally measurable.

sensing transfer function that maps the tip deflection  $p$  into the measured current  $I_R$  (Fig. 12). Note that with the experimental setup in place, it is possible to monitor the tip deflection  $p$  as well as the thermal-sensor current  $I_R$ .  $t_s = l_0 + p + t_h - z$  (see Fig. 3), and, therefore, we have  $\Delta t_s = \Delta p$  since  $z$ ,  $l_0$ , and  $t_h$  are constant. Moreover, as  $V_R$  is constant, we have  $\Delta V_{\text{esf}} = \Delta V_{\text{sub}}$ .

In the rest of this paper, we focus on experimental identification of the sensing transfer function ( $\Gamma_{\tilde{I}_R \tilde{t}_s}$ ) of the thermal sensor. This will involve the identification of the mechanical transfer function and the overall transfer function from  $V_{\text{sub}}$  to  $I_R$  ( $\Gamma_{\tilde{I}_R \tilde{V}_{\text{sub}}}$ ) as an intermediate step. Experimentally obtained  $\Gamma_{\tilde{I}_R \tilde{t}_s}$  will be compared with the one obtained from exhaustive FEM simulations to establish the validity of the proposed technique. Finally,  $H(j\omega)$  will be evaluated using (9). Methodology to obtain the thermal transfer function  $\Gamma_{\tilde{I}_R \tilde{V}_R}$  and  $C(j\omega)$  [see (8)] are the same as mentioned in [14].

#### A. Identification of Sensing Transfer Function ( $\Gamma_{\tilde{I}_R \tilde{t}_s}$ )

In this part of the paper, experimental results and procedures for identifying the dynamic map  $\Gamma_{\tilde{I}_R \tilde{t}_s}$  are presented. In related experiments, the voltage  $V_R$  is kept constant at 3 V. The sample is held fixed in the lateral direction and small-signal dynamic maps are obtained at various nominal tip-sample separations

$t_{s0}$ . The nominal tip-sample separation can be changed using a piezoelectric-actuation-based sample positioner.

The substrate voltage  $V_{\text{sub}}$  provided is sinusoidal (of the form  $A \sin(2\pi f)$ ), with 1-V peak-to-peak voltage. A sinusoidal  $V_{\text{sub}}$  with frequency at the resonant frequency  $f_0$  of the electrostatically forced cantilever results in cantilever oscillations with approximately 60-nm amplitude. These amplitudes translate to practical values for dynamic-mode operation. The thermal-sensor current  $I_R$  and the optical deflection signal  $p$  are recorded. Effectively, data is recorded with  $V_{\text{sub}} = A \sin(2\pi f)$ , for various values of  $f \in [0, 100 \text{ kHz}]$ . At each  $V_{\text{sub}}$  actuation frequency  $f$ , the measured deflection signal  $p$  and the thermal signal  $I_R$  are found to be nearly sinusoids with frequency  $f$ , with steady-state amplitudes  $|\hat{p}(j\omega)|$  and  $|\hat{I}_R(j\omega)|$  respectively. The higher harmonics are negligibly small for most of the frequency range of  $f$ . The gains  $|\hat{p}(j\omega)/A|$  and  $|\hat{I}_R(j\omega)/A|$  and their relative phase with respect to  $V_{\text{sub}}$ , thereby identifying  $\Gamma_{\tilde{t}_s \tilde{V}_{\text{esf}}}$  and  $\Gamma_{\tilde{I}_R \tilde{V}_{\text{esf}}}$  (see Figs. 12 and 14), are shown in Figs. 11 and 13.

Throughout this paper, an implicit assumption made is that the substrate voltage affects the thermal-sensor current  $I_R$  only through the tip-sample separation. Thus, it is assumed that when there is a change in  $V_{\text{sub}}$ , the electrostatic force on the cantilever changes, and, therefore, the cantilever deflection is changed, leading to a changed distance from the sample. This leads to a changed current due to the changed thermal-sensor resistance. However, the cantilever is a current path that is present in an oscillating electric field due to oscillating  $V_{\text{sub}}$ , and there is a possibility that the voltage  $V_{\text{sub}}$  directly affects the current  $I_R$  even when the tip-sample separation is unchanged (see Fig. 14). In the setup, such a direct feedthrough effect is captured through a transfer function  $\Gamma_{\tilde{I}_R \tilde{V}_{\text{esf}}}$  that relates small changes in  $V_{\text{sub}}$  to small changes in  $I_R$  without any dependence of the cantilever motion.  $\Gamma_{\tilde{I}_R \tilde{V}_{\text{esf}}}$  can be found by bringing the tip in contact with the sample and then observing the current  $I_R$  while the substrate voltage  $V_{\text{sub}}$  is changed. As the tip remains in contact with the sample,  $\Delta t_s$  remains zero. This disconnects the top path in Fig. 14 from  $\Delta V_{\text{sub}}$  to  $\Delta I_R$ . The feedthrough term can then be characterized using Fourier methods. The corresponding data obtained when the tip is in continuous contact with the sample identifies  $\Gamma_{\tilde{I}_R \tilde{V}_{\text{esf}}}$  and is shown in Fig. 15. Rise in magnitude and phase

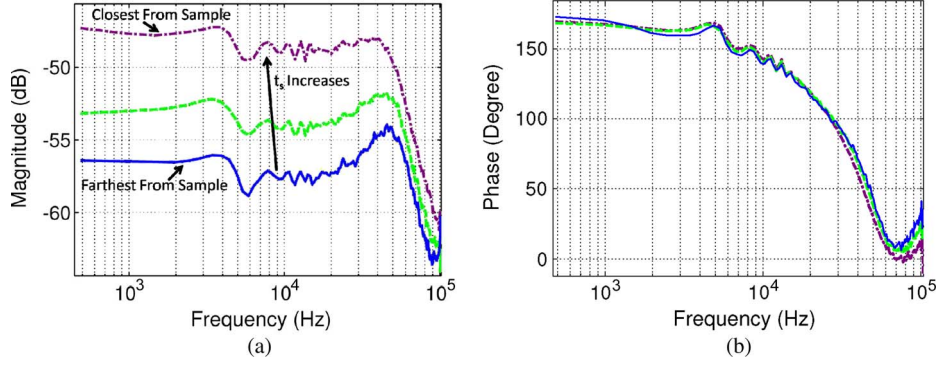


Fig. 13. Experimentally obtained (a) magnitude and (b) phase of overall transfer function from  $V_{esf}$  to  $I_R$  at various tip-sample separation (see Fig. 12). Tip-sample separation increases from top to bottom as shown in the figure.

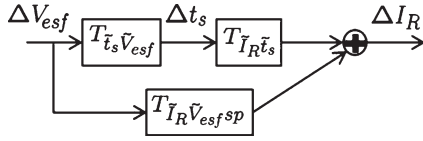


Fig. 14. Modified small signal simulation model of the system about a nominal point of operation of dynamic mode to include a direct path from  $V_{esf}$  to  $I_R$  with no dependence on  $\Delta t_s$  which is called  $\Gamma_{I_R \tilde{V}_{esf} sp}$ . This needs to be included because oscillating  $V_{esf}$  voltage gives rise to oscillation on  $I_R$  even when  $\Delta t_s = 0$ , i.e., the tip is in contact with the sample. This can possibly be attributed to the capacitive or inductive coupling between the cantilever and the sample.

at large frequencies in this transfer function indicates possible capacitive or inductive origins. This identification is used to calculate the sensing transfer function.

The sensing transfer function is determined using the relationship

$$\Gamma_{I_R \tilde{t}_s} = \frac{\Gamma_{I_R \tilde{V}_{esf}} - \Gamma_{I_R \tilde{V}_{esf} sp}}{\Gamma_{\tilde{t}_s \tilde{V}_{esf}}} \quad (11)$$

with the tip close to the sample. This relationship is obtained from Fig. 14. Note that  $\Gamma_{I_R \tilde{V}_{esf}}$ ,  $\Gamma_{I_R \tilde{V}_{esf} sp}$ , and  $\Gamma_{\tilde{t}_s \tilde{V}_{esf}}$  have been experimentally identified. Fig. 16 shows the sensing transfer function evaluated following (11) and presents a comparison with FEM simulations. The sensitivity of the thermal-sensor output close to the sample is  $102.63 \mu A/nm$ , and the bandwidth is nearly 12 kHz. The sensing transfer function has a roll-off of 10 dB/dec as expected from theoretical calculations for the thermal-sensor size under consideration [13]. Experimental identification of the sensing transfer function does not require any assumption on the form of  $\Gamma_{TP}$  once the overall block diagram (Fig. 14) is fixed.

*Remark:* Note that if the direct feedthrough term  $\Gamma_{I_R \tilde{V}_{esf} sp}$  is neglected, then the sensing transfer function can be found as

$$\Gamma_{I_R \tilde{t}_s} = \frac{\Gamma_{I_R \tilde{V}_{esf}}}{\Gamma_{\tilde{t}_s \tilde{V}_{esf}}} \quad (12)$$

Such an evaluation results in  $\Gamma_{I_R \tilde{t}_s}$  as shown in Fig. 17. This agrees with the sensing transfer function shown in Fig. 16 where the feedthrough term is not neglected except for the high frequency rise where Fig. 17 shows a rise in magnitude. Such a rise is not corroborated by the existing analysis and FEM

simulations. The conclusion is that the feedthrough term affects the high frequency region only and can be neglected if such a frequency region is not of interest.

### B. Identification of $H(j\omega)$

We now seek to determine  $H(j\omega)$ , the dynamic map between  $t_s$  and temperature  $T$ , experimentally. Toward this goal, input perturbations of approximately 200 mV are introduced at  $V_R$  about a nominal point of  $V_{R0} = 3$  V, and  $I_R$  is recorded. At this stage,  $g(T)$  and  $g'(T)$  are known from the methods described in Section III. Fig. 18 shows the experimentally evaluated  $C(j\omega)$  using the methods outlined in [14] when the tip is close to the sample. It shows that  $C(j\omega)$  has a low-pass characteristics with roughly 10-dB/dec drop as expected for the thermal-sensor size under consideration [13]. The power-to-temperature conversion factor when the cantilever is close to the sample, represented by the dc gain of  $C(j\omega)$ , is  $111^\circ C/mW$ , and the bandwidth is roughly 12 kHz.

A method to evaluate  $H(j\omega)$  is to use a nonlinear model (Fig. 20) where we assume that data  $\Delta t_s$  (measured optically) and  $I_R$  are recorded, and  $V_R$  is kept constant at a nominal value  $V_{R0}$ . At this stage,  $C(j\omega)$  and  $g(T)$  have been obtained experimentally. From the measurement of  $I_R$ ,  $\Delta P = V_{R0} I_R - P_0$ ,  $\Delta T = g^{-1}(V_{R0}/I_R) - g^{-1}(R_0)$ , and  $\Delta T_1 = \Delta T - \Gamma^{-1}(C(j\omega)) * \Delta P$  can be obtained, where  $R_0$  and  $P_0$  are the mean value of the resistance and power,  $T_1$  is the output of  $H(j\omega)$  block, and  $\Gamma^{-1}(C(j\omega)) * \Delta P$  is the inverse Fourier transform of the  $C(j\omega)$  convolved with  $\Delta P$ . Thus,  $H(j\omega)$  can be evaluated as  $H(j\omega) = C_{T_1 \tilde{t}_s}(j\omega)/C_{\tilde{t}_s \tilde{t}_s}(j\omega)$ , where  $C_{T_1 \tilde{t}_s}(j\omega)$  denotes the cross covariance between  $\Delta t_s$  and  $\Delta T_1$ , and  $C_{\tilde{t}_s \tilde{t}_s}(j\omega)$  denotes the autocovariance of  $\Delta t_s$ . Fig. 19 shows the experimentally obtained  $H(j\omega)$  when the tip is close to the sample. DC gain of  $H(j\omega)$  is a positive value which increases with reducing tip-sample separation. Positiveness comes from the fact that a small reduction in  $t_s$  about a nominal point will further reduce the cantilever temperature. The increase in the dc gain with reducing tip-sample separation reflects an increase in sensitivity with reducing tip-sample separation.

At this stage, methods to obtain sensing transfer function of the thermal sensor and  $H(j\omega)$  are validated.  $C(j\omega)$  and the thermal transfer function,  $\Gamma_{I_R \tilde{V}_R}$  are obtained using the methods

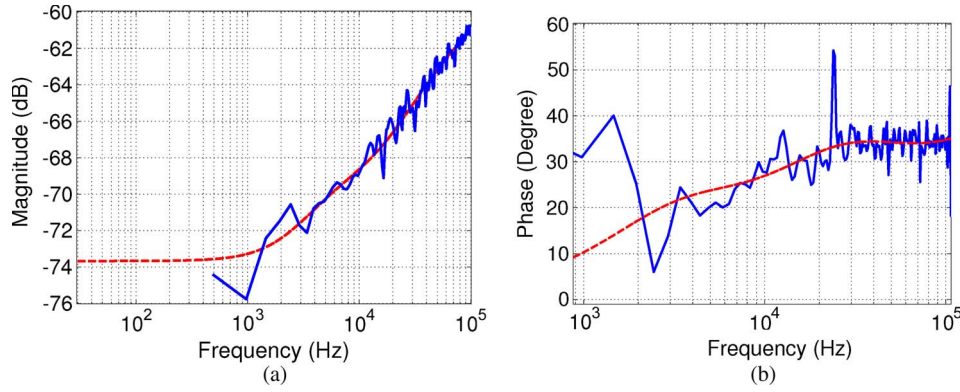


Fig. 15. Experimentally obtained magnitude and phase of  $\Gamma_{\tilde{I}_R \tilde{V}_{esfsp}}$  close to the sample. (a) Magnitude (b) Phase. Blue-solid: experimental; red-dashed: transfer function fit to the data. Rise in magnitude and phase with frequency suggests of possible capacitive or inductive origins to this component of  $\Delta I_R$  due to changes in  $V_{esf}$ .

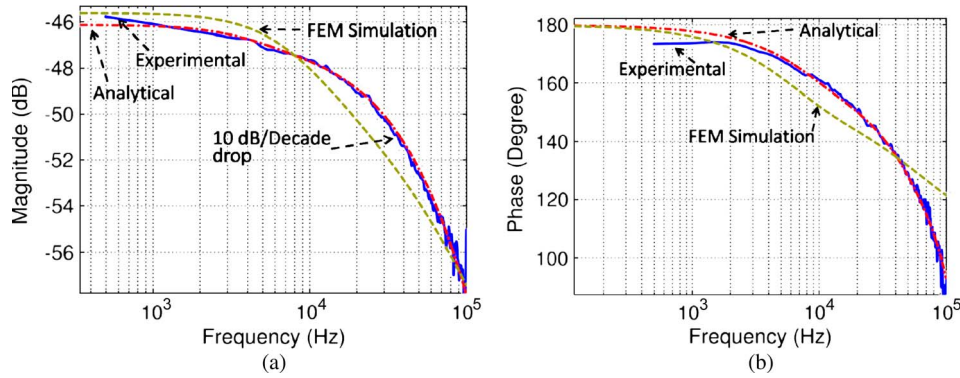


Fig. 16. Experimentally obtained magnitude and phase of sensing transfer function due to heat-conduction processes. (a) Magnitude (b) Phase. Solid-blue: experimentally obtained without assuming any model for the thermal sensor using (11); dashed-green: FEM Simulations; red-dashed/dot: obtained from (7) and experimentally obtained  $H(j\omega)$ . The experimentally obtained sensing transfer function matches with the results obtained from FEM simulations both in magnitude and phase. A 10-dB/dec drop at higher frequencies and a bandwidth of approximately 12 kHz is as expected from theoretical predictions.

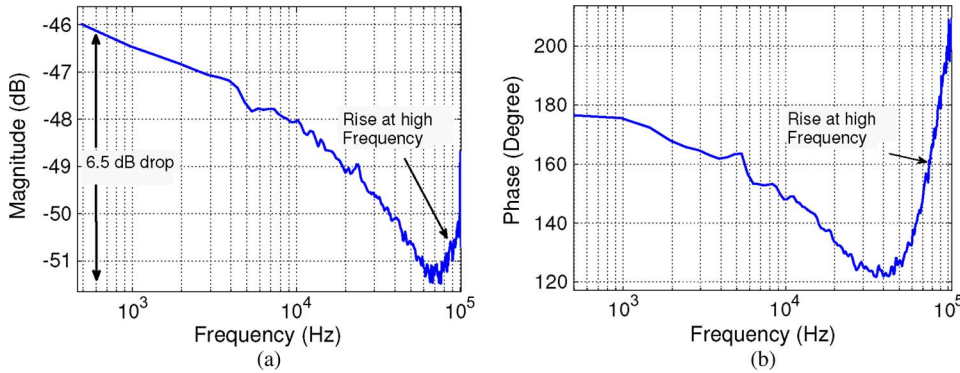


Fig. 17. Experimentally obtained magnitude and phase of transfer function from  $t_s$  to  $I_R$  using (12) at a tip-sample separation close to zero. The total drop in magnitude plot from 0 to 100 kHz is around 5–6 dB, and there is also a rise in magnitude and phase at high frequency. This is not in agreement with the theoretical predictions for the considered cantilever geometry.

outlined in [14]. Thus, dynamic model of thermal sensor as shown in Figs. 10, 12, 14, and 20 is characterized.

$H(j\omega)$  evaluated in this manner can be substituted in (7) to obtain one estimate of sensing transfer function  $\Gamma_{\tilde{I}_R \tilde{t}_s}$ . This estimate can be compared with the experimentally obtained sensing transfer function  $\Gamma_{\tilde{I}_R \tilde{t}_s}$ , assuming no models and using (11). Such a comparison is shown in Fig. 16. The blue-solid curve is the experimentally identified sensing transfer function assuming no models and (11), whereas the red-dashed curve

represents the sensing transfer function estimated using (7) and experimentally obtained  $H(j\omega)$ . There is a good agreement between the magnitude and phase response of the sensing transfer function using (7) and experimentally obtained  $H(j\omega)$  and the sensing transfer function estimated assuming no models (see (11) and Fig. 16). This indicates that linearization of the  $\Gamma_{TP}$  operator and other nonlinear operators in the thermal sensor accurately capture the system response to small input perturbations at  $V_{sub}$ .





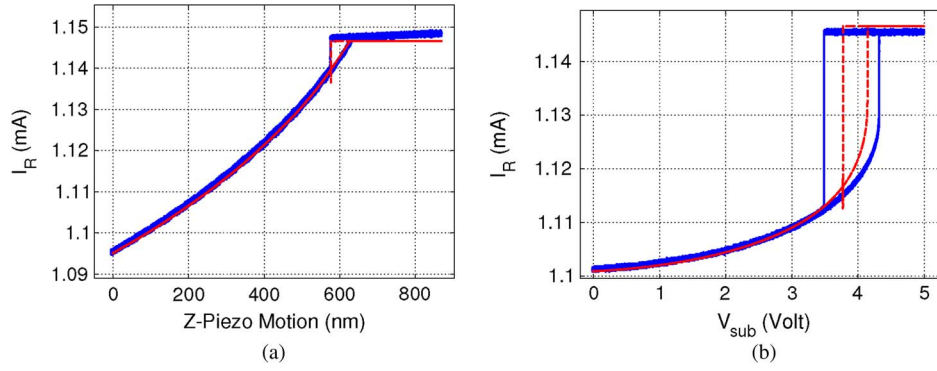


Fig. 21. (a)  $z$  force curve plotted between thermal-sensor output  $I_R$  and  $z$ -piezo motion  $z_s$ . (Solid-blue) Experimental curves agree well with the (dashed-red) simulated curves indicating that the tip-sample interaction model is able to capture snap-in and snap-off points and the slope in the repulsive region for tip interacting with the polymer sample. Quasi-static dependence of  $\Gamma_{TP}$  on  $t_s$  is calibrated well. (b) Electrostatic-force curve plotted between the thermal-sensor output  $I_R$  and substrate voltage  $V_{sub}$ . Blue solid line is experimental; red dashed line is simulation. The electrostatic-force curves agree quantitatively when the tip is far from the sample but tend to deviate slightly near the sample because the parallel-plate capacitor model for  $F_{esf}$  is not very accurate near the sample.

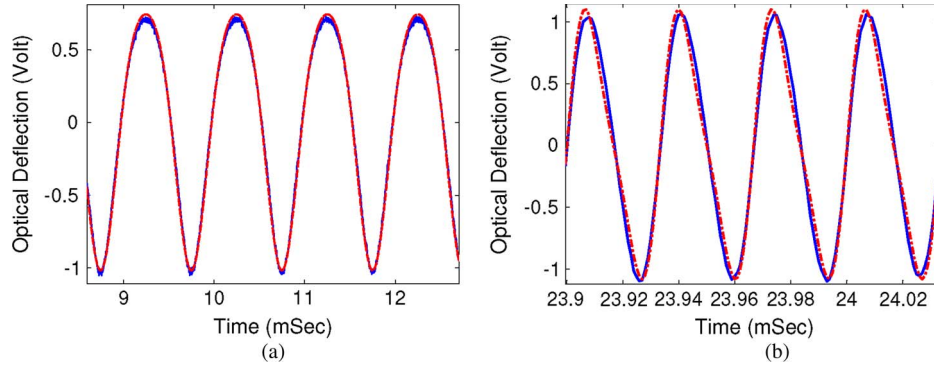


Fig. 22. (Blue-solid curve) Experimental and (red-dashed curve) simulated noninteracting cantilever trajectories that are sensed optically are shown. (a) Cantilever response to 1-kHz sine  $V_{sub}$  actuation measured optically (b) Cantilever response to 30-kHz sine  $V_{sub}$  actuation measured optically. In these trajectories, the tip is not interacting with the sample. Nominal distance of the tip from the sample is approximately 70 nm. Cantilever trajectories are nonsinusoidal but periodic at low actuation frequencies. They tend to become sinusoidal at higher actuation frequencies because higher harmonics are filtered by the cantilever  $G(j\omega)$ .

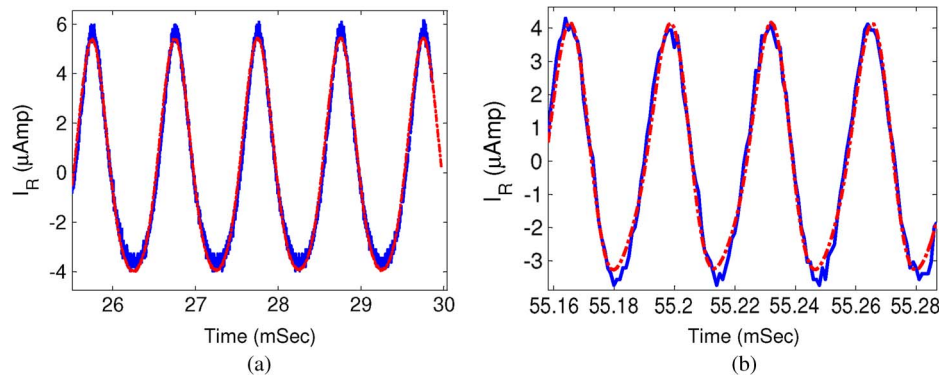


Fig. 23. (Blue-solid curve) Experimental and (red-dashed curve) simulated noninteracting cantilever trajectories that are sensed thermally are shown. (a) Cantilever response to 1-kHz sine  $V_{sub}$  actuation measured thermally (b) Cantilever response to 30-kHz sine  $V_{sub}$  actuation measured thermally. Quantitative agreement between the simulated and the experimental trajectories at various frequencies indicates that experimental characterization of the thermal sensing transfer function is accurate.

tip-sample interaction forces, adhesive, and meniscus forces is accurate enough to capture important system behavior due to these forces. Thermal electrostatic force curve is shown in Fig. 21(b) where a good quantitative agreement is obtained when the tip is away from the sample. Snap-in and snap-off instances of electrostatic force curves are not accurately captured, and off-sample agreement indicates that an assumption

of parallel plates for the electrostatic-force model accurately predicts off-sample system behavior.

The model shown in Fig. 20 is simulated for various  $V_{sub}$  profiles. It is seen that noninteracting optical and thermal trajectories are quantitatively predicted by simulations (see Figs. 22 and 23). Quantitative agreement between the simulated and experimental trajectories indicates that even though the  $F_{esf}$

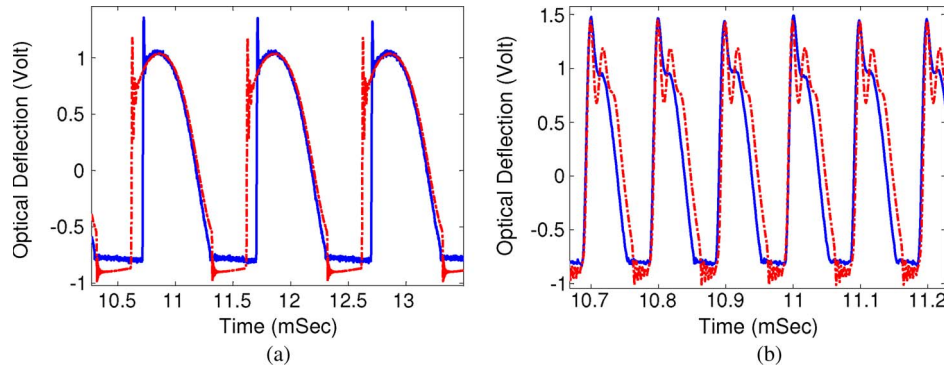


Fig. 24. (Blue-solid curve) Experimental and (red-dashed curve) simulated interacting cantilever trajectories that are sensed optically is shown. (a) Cantilever response to 1-kHz sine  $V_{\text{sub}}$  actuation measured optically. (b) Cantilever response to 10-kHz sine  $V_{\text{sub}}$  actuation measured optically.

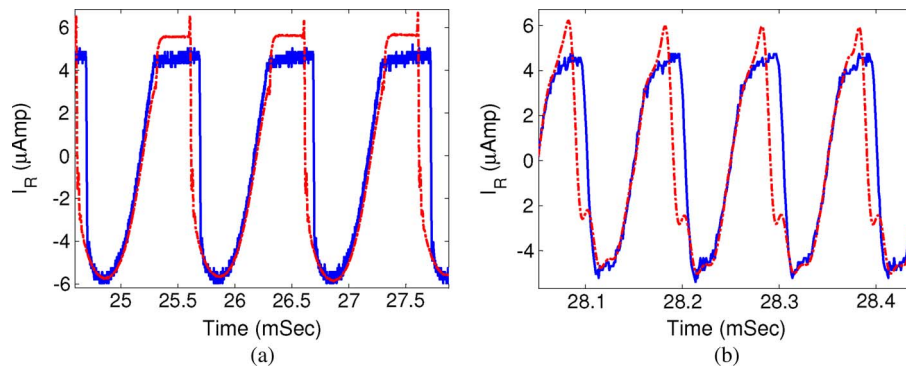


Fig. 25. (Blue-solid curve) Experimental and (red-dashed curve) simulated interacting cantilever trajectories that are sensed thermally is shown. (a) Cantilever response to 1-kHz sine  $V_{\text{sub}}$  actuation measured thermally. (b) Cantilever response to 10-kHz sine  $V_{\text{sub}}$  actuation measured thermally. These trajectories result from tip interaction with the sample at a single point. At low actuation frequencies, snap-in and snap-off points are present in each oscillation cycle, whereas their effect reduces as the actuation frequency increases. Interacting trajectories also become sinusoidal at higher actuation frequencies.

model (3) is not accurate for modeling quasi-static behavior near the sample, it is still able to quantitatively predict the overall trajectories near the sample. Periodic  $V_{\text{sub}}$  at low excitation frequencies yield  $I_R$  trajectories that are not sinusoidal, and the model is able to predict the phase and magnitude of harmonics to get a quantitative match. As the excitation frequency of  $V_{\text{sub}}$  is increased, the trajectories of  $I_R$  become sinusoidal because the cantilever mechanical response  $G(j\omega)$  filters the higher harmonics of the input excitation effectively. Linearized models (6)–(10) can thus be used at high actuation frequencies when the trajectories are near sinusoidal, while a nonlinear model is required for lower actuation frequencies for good prediction of experimental trajectories.

Interacting trajectories obtained by allowing the tip to interact with the sample at a single point for 1 kHz and 10 kHz input excitation sinusoids are shown to agree with simulations (see Figs. 24 and 25). Interacting trajectories are also periodic and nonsinusoidal at low frequencies. These trajectories have more nonlinearities, i.e., have more harmonics, as compared with noninteracting trajectories because they are also affected by the nonlinear tip-sample interaction force in addition to the electrostatic force. The model accurately predicts the change in harmonics with the input frequency. Interacting trajectories also become sinusoidal at higher excitation frequencies. Thus, the model is accurate for on-sample and off-sample behavior of electrostatically actuated cantilever with integrated solid-state

thermal sensor. The model is also able to predict quasi-static large input signal behavior of the system accurately. Quantitative agreement of the thermal-sensor output for different input signals indicate that lumped parameter modeling for the thermal sensor accurately predicts its behavior.

## VI. CONCLUSION

This paper has presented a comprehensive modeling paradigm for a MEMS cantilever that is electrostatically actuated and has an integrated thermal sensor for topography measurement. It also provides a precise means of identifying model parameters. The proposed methodology is corroborated with experimental data to determine the reasonableness of the assumptions made in the modeling and identification procedures. It is evident that system approach to modeling a MEMS cantilever that interacts with the tip-sample potential and the electrostatic forces provides an efficient means of predicting experimental data. A significant conclusion is that model parameters can be identified using thermal-sensor data alone. This paper further presents for the first time an experimentally obtained sensing transfer function due to heat-conduction processes until a bandwidth of 100 kHz for an integrated solid-state heater. A good match with FEM simulations is shown. A significant outcome of this paper is a reliable simulation model that obviates the need for elaborate experimental validation.



## ACKNOWLEDGMENT

The authors would like to thank C. Hagleitner for providing the FEM simulation results for the device under study, and P. Bächtold, W. Häberle, D. Wiesmann, and A. Pantazi of the Probe Storage Group, IBM Zürich Research Laboratory, for their contributions to this work.

## REFERENCES

- [1] W. P. King, S. Saxena, and B. A. Nelson, "Nanoscale thermal analysis of an energetic material," *Nano Lett.*, vol. 6, no. 9, pp. 2145–2149, Sep. 2006.
- [2] B. A. Nelson, W. P. King, A. R. Laracuente, P. E. Sheehan, and L. J. Whitman, "Direct deposition of continuous metal nanostructures by thermal dip-pen nanolithography," *Appl. Phys. Lett.*, vol. 88, no. 3, p. 033104, Jan. 2006.
- [3] K. Park, J. Lee, Z. M. Zhang, and W. P. King, "Topography imaging with a heated atomic force microscope cantilever in tapping mode," *Rev. Sci. Instrum.*, vol. 78, no. 4, p. 043709, Apr. 2007.
- [4] K. J. Kim, K. Park, J. Lee, Z. M. Zhang, and W. P. King, "Nanotopographical imaging using a heated atomic force microscope cantilever probe," *Sens. Actuators A, Phys.*, vol. 136, no. 1, pp. 95–103, May 2007.
- [5] E. O. Sunden, T. L. Wright, J. Lee, W. P. King, and S. Graham, "Room-temperature chemical vapor deposition and mass detection on a heated atomic force microscope cantilever," *Appl. Phys. Lett.*, vol. 88, no. 3, p. 033107, Jan. 2006.
- [6] A. S. Basu and Y. B. Gianchandani, "Shaping high-speed Marangoni flow in liquid films by microscale perturbations in surface temperature," *Appl. Phys. Lett.*, vol. 90, no. 3, p. 034102, Jan. 2007.
- [7] D. Lange, T. Akiyama, C. Hagleitner, A. Tonin, H. R. Hidber, P. Niedermann, U. Staufer, N. F. De Rooij, O. Brand, and H. Baltes, "Parallel scanning AFM with on-chip circuitry in CMOS technology," in *Proc. 12th IEEE Int. Conf. MEMS*, 1999, pp. 447–452.
- [8] A. Majumdar, "Scanning thermal microscopy," *Annu. Rev. Mater. Sci.*, vol. 29, pp. 505–585, 1999.
- [9] E. Eleftheriou, T. Antonakopoulos, G. K. Binnig, G. Cherubini, M. Despont, A. Dholakia, U. Dürig, M. A. Lantz, H. Pozidis, H. E. Rothuizen, and P. Vettiger, "Millipede—A MEMS-based scanning-probe data-storage system," *IEEE Trans. Magn.*, vol. 39, no. 2, pp. 938–945, Mar. 2003.
- [10] A. Passian, R. J. Warmack, T. L. Ferrell, and T. Thundat, "Thermal transpiration at the microscale: A Crookes cantilever," *Phys. Rev. Lett.*, vol. 90, no. 12, p. 124 503, Mar. 2003.
- [11] W. P. King, "Design analysis of heated atomic force microscope cantilevers for nanotopography measurements," *J. Micromech. Microeng.*, vol. 15, no. 12, pp. 2441–2448, Nov. 2005.
- [12] J. Lee, T. L. Wright, M. R. Abel, E. O. Sunden, A. Marchenkov, S. Graham, and W. P. King, "Thermal conduction from microcantilever heaters in partial vacuum," *J. Appl. Phys.*, vol. 101, no. 1, p. 014906, Jan. 2007.
- [13] U. Dürig, "Fundamentals of micromechanical thermoelectric sensors," *J. Appl. Phys.*, vol. 98, no. 4, p. 044906, Aug. 2005.
- [14] A. Sebastian and D. Wiesmann, "Modeling and experimental identification of silicon microheaters: A systems approach," *J. Microelectromech. Syst.*, vol. 17, no. 4, pp. 911–920, Aug. 2008.
- [15] C. Dames and G. Chen, " $1\omega$ ,  $2\omega$  and  $3\omega$  methods for measurements of thermal properties," *Rev. Sci. Instrum.*, vol. 76, no. 12, p. 124 902, Dec. 2005.
- [16] P. O. Chapuis, J. J. Greffet, K. Joulain, and S. Volz, "Heat transfer between a nano-tip and a surface," *Microelectron. Eng.*, vol. 67/68, pp. 2978–2981, 2003.
- [17] J. Kim, S. G. Kim, J. G. Koo, T. M. Roh, H. Soopark, and D. Y. Kim, "Characteristics of dynamic resistance in a heavily doped silicon semiconductor resistor," *Int. J. Electron.*, vol. 86, no. 3, pp. 269–279, Mar. 1999.
- [18] B. W. Chui, M. Asheghi, Y. S. Ju, K. E. Goodson, T. W. Kenny, and H. J. Mamin, "Intrinsic-carrier thermal runaway in silicon microcantilevers," *Microscale Thermophys. Eng.*, vol. 3, no. 3, pp. 217–228, Aug. 1999.
- [19] D. R. Sahoo, W. Häberle, P. Bächtold, A. Sebastian, H. Pozidis, and E. Eleftheriou, "On intermittent-contact read operation in a MEMS-based scanning probe data-storage system," in *Proc. Amer. Control Conf.*, Jun. 2008, pp. 2034–2039.
- [20] Q. Zhong, D. Inniss, K. Kjoller, and V. B. Elings, "Fractured polymer/silica fiber surface studied by tapping mode atomic force microscopy," *Surf. Sci. Lett.*, vol. 290, no. 1/2, pp. L688–L692, Jun. 1993.
- [21] A. Sebastian, M. V. Salapaka, D. Chen, and J. P. Cleveland, "Harmonic and power balance tools for tapping-mode atomic force microscope," *J. Appl. Phys.*, vol. 89, no. 11, pp. 6473–6480, Jun. 2001.
- [22] P. Vettiger, G. Cross, M. Despont, U. Drechsler, U. Dürig, B. Gotsmann, W. Häberle, M. A. Lantz, H. E. Rothuizen, R. Stutz, and G. K. Binnig, "The "Millipede"—Nanotechnology entering data storage," *IEEE Trans. Nanotechnol.*, vol. 1, no. 1, pp. 39–55, Mar. 2002.
- [23] P. Agarwal, D. R. Sahoo, A. Sebastian, H. Pozidis, and M. Salapaka, "Modeling and identification of the dynamics of electrostatically actuated microcantilever with integrated thermal sensor," in *Proc. Conf. Decision Control*, Dec. 2008, pp. 2624–2630.
- [24] A. F. Marques and A. M. Shkel, "On electrostatic actuation beyond snapping condition," in *Proc. IEEE Sens.*, Oct. 2005, pp. 600–603.
- [25] K. Madsen, H. B. Nielsen, and O. Tingleff, "Methods for non-linear least squares problems," Tech. Univ. Denmark, Copenhagen, Denmark, 2004.



**Pranav Agarwal** received the B.Tech. degree in electrical engineering from the Indian Institute of Technology, Kanpur, India, in 2000, and the M.S. degree in electrical engineering from Iowa State University, Ames, in 2007. He is currently working toward the Ph.D. degree at the University of Minnesota–Twin Cities, Minneapolis.

He worked as a Design Engineer with ST Microelectronics, Noida, India, until 2004, where he was involved in digital design of sigma-delta data converters. His research interests include developing

high bandwidth techniques for material characterization at nanoscale, quantitative imaging and signal processing algorithms involving probe-based sensors, and study of dynamics and control of processes at nanoscale.



**Deepak R. Sahoo** received the B.Tech. (Hons.) degree in energy engineering from the Indian Institute of Technology, Kharagpur, India, in 2000, and the Ph.D. degree in electrical engineering from Iowa State University, Ames, in 2006.

During his Ph.D. studies, he worked on the control of quantum-mechanical systems as well as real-time operating systems, and developed a high-speed model-based imaging technique for scanning-probe microscopy. He is currently a Postdoctoral Researcher with the IBM Zürich Research Laboratory, Rüschlikon, Switzerland.

At IBM, he has developed a high-speed and minimally invasive operation technique for parallel scanning-probe-based MEMS devices. He is currently working on high-bandwidth sensing and actuation of microcantilevers for scanning-probe microscopy. His research interests include dynamics, control, and signal processing.



**Abu Sebastian** (M'03) received the B.E. (Hons.) degree in electrical and electronics engineering from Birla Institute of Technology and Science, Pilani, India, in 1998, and the M.S. and Ph.D. degrees in electrical engineering from Iowa State University, Ames, in 1999 and 2004, respectively.

He is currently a Research Staff Member with the IBM Zürich Research Laboratory, Rüschlikon, Switzerland. Recently, he has been involved in the development of the first scanning-probe-based data-storage device prototype. His research is focused on dynamics and control at the nanometer scale. His research interests include microcantilever-based devices and enabling technologies like nanometer-scale sensing and nanopositioning.

Dr. Sebastian currently serves on the Technical Committee on Mechatronics of the International Federation of Automatic Control and on the Editorial Board of the journal *Mechatronics*.



**Haris Pozidis** (M'98) received the Diploma degree in computer engineering and informatics from the University of Patras, Patras, Greece, in 1994, and the M.Sc. and Ph.D. degrees in electrical engineering from Drexel University, Philadelphia, PA, in 1997 and 1998, respectively.

Between 1998 and 2001, he was with Philips Research, Eindhoven, The Netherlands, where he worked on read-channel design for optical storage devices, in particular, DVD rewritable and Blu-ray Disc formats. Since 2001, he has been with the

IBM Zürich Research Laboratory, Rüschlikon, Switzerland, working on basic recording technology, signal processing, and system-level design for MEMS-based scanning-probe data-storage devices. He currently manages a group that focuses on novel nonvolatile-memory concepts and applications of scanning probes to nanoscale investigation.



**Murti V. Salapaka** received the B.Tech. degree in mechanical engineering from the Indian Institute of Technology, Madras, India, in 1991, and the M.S. and Ph.D. degrees in mechanical engineering from the University of California, Santa Barbara, in 1993 and 1997, respectively.

He was a Faculty Member in the Electrical and Computer Engineering Department, Iowa State University, Ames from 1997 to 2007. Currently, he is a Faculty Member in the Electrical and Computer Engineering Department, University of

Minnesota–Twin Cities, Minneapolis. His research interests are nanotechnology, multiple-objective robust control, and distributed and structural control.

Dr. Salapaka was the recipient of a 1997 National Science Foundation CAREER Award.